Journal of Ovonic Research Vol. 14, No. 6, November - December, p. 415 - 427

SYNTHESIS AND CHARACTERIZATION OF SILVER DOPED ZnO NANOPARTICLES FOR HYDROGEN PRODUCTION

I. AHMAD[a], E. AHMED[b], M. ULLAH [a,*], A. M. RANA[a], M. F. MANZOOR[a], M. A. RASHEED[a], A. S. MALIK[c], N. R. KHALID[d], M.AHMAD[a], U. MEHTAB[e]

[a]Department of Physics, Bahauddin Zakariya University, Multan-60800, Pakistan
[b]Department of Physics, University of Central Punjab(UCP), Lahore
[c]Department of Electrical engineering, B.Z. University Multan
dDepartment of Physics university of Gujrat, Gujrat 320700
[e]Faculty of veterinary Science, B.Z. University Multan.

Silver doped ZnO nanoparticles for hydrogen production were synthesized using auto-combustion technique and investigated using X-ray diffraction (XRD), scanning electron microscopy (SEM), photoluminescence (PL) spectroscopy, diffuse reflectance spectroscopy (DRS) etc. The polycrystalline structure of silver doped ZnO was confirmed by XRD patterns. SEM was used to reveal the surface information and particle morphology of these composites. There is a direct band gap for silver doped ZnO nanoparticles which reduces with doping concentration of silver as confirmed by DRS. The PL study indicates that there is a reduction in PL intensity with silver doping, exhibiting lower rate of electron-hole recombination. Also there is a decrement in the dielectric constant and dielectric loss with silver content and reverse trend is noticed for AC conductivity. The electrical measurements demonstrate reduction in DC conductivity with silver doping. Cyclic voltammetry (CV) measurements indicate oxidation and reduction reactions which seems suitable for hydrogen production.

(Received August 15, 2018; Accepted November 13, 2018)

Keywords: ZnO nanoparticles, Hydrogen Production, silver, Energy band, Dielectric Properties

1. Introduction

The photocatalytic hydrogen production from water is a demanding technique which employs the process of semiconductor photocatalysis and has become a popular way for producing energy in the last decade. The major sources of producing hydrogen energy involve solar energy's pyrogenic decomposition, solar energy in combination with electrolytic method, photocatalytic phenomena and photoelectrochemistry techniques [1-5]. For this purpose, a lot of semiconducting materials have been investigated. However, many of these materials possess wide band gap due to which photons are produced in the ultraviolet region of the solar spectrum [6-7]. Among these materials, ZnO belongs to the family of n-type semiconductors and has a wide band gap of 3.37 eV, large exciton binding energy of 60 meV at room temperature and hexagonal wurtzite structure possessing lattice parameters of a = 0.325 nm and c = 0.521 nm with c/a ratio of 1.6 [8]. Because of these characteristics, ZnO has wide applications in the fields of gas sensors, solar cells, spintronics, photonic devices, light emitting devices, surge suppressors, ceramics and transducers etc. [9]. In addition, it is a biocompatible, biosafe and phototoxic intercellular compound. When it is doped with transition metals at room temperature it displays so many applications including n-type nanolaser, ferromagnetic semiconducting nanomaterials etc. [10]. The transition metals doping also enhances the optical, magnetic and electrical properties of ZnO. The elements of group-II can be used as possible dopants for ZnO and silver is selected because of its role in generating shallow acceptor levels in ZnO [11]. Due to high stability and compatibility with transparent and conducting oxides at high temperature, Ag-doped ZnO is utilized in optoelectronic applications. Moreover, silver assists in achieving better luminescence efficiency [12].

When light of photon energy equal or greater than the band gap energy of a semiconductor is irradiated, generation of electrons and holes takes place in the conduction and valence band of the

---

[*] Corresponding author: mahtabullah@yahoo.com

photocatalyst respectively. The electrons join with H^+ to form atomic hydrogen and holes react with water to produce atomic oxygen. The presence of a number of active sites on the surface assist in enhancing these reactions and hence larger surface area of a catalyst becomes advantageous for the catalytic process. That is why, the photocatalytic performance of a semiconducting material relies on the electron-hole recombination rate and adsorption ability of solar radiations. The light adsorption ability can be increased by the modification of energy band gap of a material [13-14] as well as creating surface texture that helps in improving light capturing impacts [15-17]. The efficiency of a photocatalyst can be improved by preventing recombination rate of the electron-hole pairs [18]. Such rate of charge recombination can be inhibited by doping metallic species. An improvement in the photocatalytic efficiency of the semiconducting materials can be made by variations in their surface characteristics [19-20]. It is possible to create a dual layer and hence the rearrangement of charges at the metal-semiconductor interface [21]. In addition, doping of metallic specie helps in producing a distance between photogenerated carriers during the process of photocatalysis [22]. Various types of dopants have been utilized to enhance the phenomenon of photocatalysis. Ranjit *et al.* have studied that complexes with different Lewis bases can be formed by the ions possessing 4f-electrons configurations. Moreover, performance of hydrogen production can be enhanced by the reaction of photo-induced holes and electron donors acting as sacrificial agents [23]. Peng *et al.* have reported that sulfide ions could be utilized as electron donors for good hydrogen production [24]. The f-state electrons of II-VI compounds are either partially occupied or empty to create the stable oxidation states. Such distinct characteristics of silver have emerged from its ability of undergoing quick and reoccurring redox processes. This property relies in the production and diffusion of oxygen vacancies, particularly on the silver surfaces [25].

In the present work, photocatalytic hydrogen production from silver doped ZnO has been investigated. This paper provides detail about preparation, structural, morphological, optical and dielectric properties of Ag-ZnO nanoparticles for hydrogen production.

2. Experimental

2.1. Preparation of Ag-ZnO nanoparticles

In this work all chemicals and reactants were used in the same form in which they were received. Silver doped ZnO nanoparticles having composition of Ag_x-ZnO_{1-x} (x= 0, 0.05, 0.1, 0.2, 0.3, 0.5) with fuel to oxidant ratio of $\Psi = 1.7$ were synthesized by a facile auto-combustion method. At first reagent grade zinc nitrate [$Zn(NO_3)_2.6H_2O$], silver nitrate [$Ag(NO)_3$] and glycine [NH_2CH_2COOH] were mixed in the desired ratio and kept in the open atmosphere for moisture absorption to form a paste like material. Then this paste was stirred with heating at 120 °C for making the solution homogeneous. On further heating at 210 °C and stirring again, the mixture was turned into gel form and after some time, this gel suddenly burst into powder with the liberation of gases. On cooling to room temperature, a powder was obtained which was calcined at 700 °C for 3 hours. A fine nanopowder was achieved which was characterized for its suitability for potential applications. Fig. 1 displays a flow chart for the preparation of Ag-doped ZnO nanoparticles. The following chemical reaction was proposed to occur during this fabrication process.

$$Zn(NO_3)_2.6H_2O + AgNO_3 \xrightarrow{\text{Glycine}} Zn_{1-x}\,Ag_xO + \text{gaseous products}$$

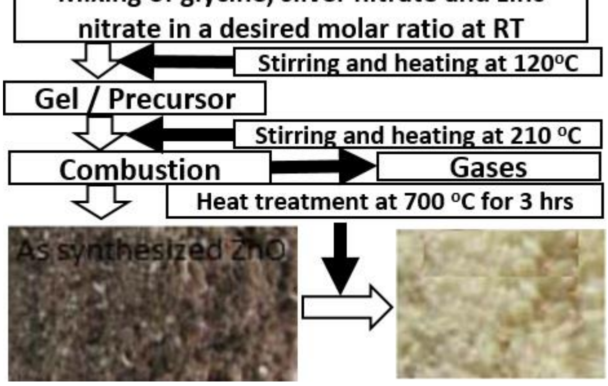

Fig. 1. Flow chart for the fabrication of Ag-ZnO nanoparticles.

2.2. Characterization techniques

Powder XRD patterns were obtained at room temperature in the 2θ range from 20° to 80° with the help of Panalytical Empyrean diffractometer equipped with CuKα radiations ($\lambda = 0.15406$ nm). The scanning electron microscope (HITACHI S-4800) was used to investigate the surface morphology and the crystallite size. The use of ultraviolet-visible spectrometer (HITACHI, U-4100) accompanied with integrating sphere accessory enabled to measure the diffuse reflectance spectroscopy (DRS) in the wavelength range of 300-800 nm. The absorbance was obtained by the conversion of the reflectance with the help of the Kubelka-Munk function $F(R)\ \alpha\ K/S = (1-R^2)/2R$, where K denotes absorption coefficient, S scattering coefficient and R indicates the diffuse reflectance. The photoluminescence PL emission spectra were recorded by applying a Hitachi F-4500 fluorescence spectrophotometer in the range of 250-700 nm. Dielectric properties were investigated by two probe method using GW-INSTEK LCR 8101 in the frequency range of 20 Hz to 1 MHz while electrical properties were measured by 2400 source meter by Keithley using LabTracer 2.8 software in the temperature range 25 °C to 125 °C. Cyclic voltammetry was studied to observe the electrochemical response of Ag-doped ZnO nanoparticles by using Autolab PGSTAT204 apparatus. Cyclic voltammetry measurements were recorded both for undoped and Ag-doped ZnO samples at scan rates of 5.0 mVs^{-1}, 10.0 mVs^{-1}, and 20.0 mVs^{-1} by immersing glassy carbon electrode (GCE) in 0.1 M NaOH electrolytic solution. The GCE acted as working electrode while Ag/AgCl was used as reference electrode. It was noted that both ZnO and Ag-ZnO systems exhibited oxidation and reduction peaks. The onset potential in the range of -1.0 V to 1.0 V was provided to estimate the current.

3. Results and discussion

3.1. X-ray diffraction

The XRD patterns of the synthesized ZnO and Ag-ZnO nanoparticles exhibited the presence of hexagonal wurtzite structure [26] as shown in Fig. 2. The broad and sharp peaks were located at 2θ values of 31.59°, 34.38° and 36.24° corresponding to (100), (002) and (101) peaks accompanied by other weak reflections which are located at 47.64°, 56.65°, 62.96°, 66.26°, 68.07°, 69.26°, 72.60° and 77.07° corresponding to (102), (110), (103), (200), (112), (201), (004) and (202) respectively. These reflections are in good agreement with those of JCPDS card # 36-1451 and previous studies [27, 28]. The lattice parameters a = 3.24982 Å and c = 5.20661 Å with c/a ratio of 1.602 were found as given by JCPDS for the hexagonal zinc oxide structure [27]. Along with these reflections, two secondary phase reflections were also observed at 2θ = 38.40°, 44.35° representing (111) and (200) planes caused by the elemental growth of silver (Ag) in agreement with JCPDS card # 04-0783.

It is noticed that there is an increase in the maximum diffraction peak intensity as well as a slight shift in peak position of (101) peak towards higher 2θ values with rising silver concentration as illustrated by Fig. 3. This behavior reveals that Ag-doping improves the crystal quality, particle size and lattice parameters. The crystallite (particle) size was calculated by estimating full width at half maximum (FWHM) of the sharp and intense (101) peak using Scherrer formula [29]:

$$d = 0.9\ \lambda/\beta \cos\theta$$

Where "d" represents the particle size, "λ" wavelength in nanometer, "β" FWHM measured in radians and "θ" Bragg angle in radians. When Ag-doping content was increased, the crystallite size of Ag-ZnO nanoparticles also increased from 41.70 nm to 51.12 nm (~22.59% increase) as shown in Table 1. XRD data reveals that silver occupies two places: (1) it substitutes Zn^{+2} in the zinc oxide lattice for small Ag concentrations, (2) it occupies interstitial sites for higher Ag contents. This is due to large ionic radii difference of silver (1.22 Å) and Zn^{+2} (0.74 Å) ions [30]. The lattice constants 'a' and 'c' of hexagonal wurtzite structure can be calculated by following equations [31]:

$$1/(d_{hkl})^2 = 4/3[\ (h^2 + hk + k^2)/\ a^2] + l^2/\ c^2$$

$$c = \lambda / \sin\theta, \qquad a = \lambda / (3^{1/3} \sin\theta)$$

Table 1. Physical parameters of ZnO and Ag-doped ZnO nanoparticles.

Sr. No .	Samples Name	I_{max} (a.u)	2θ at (I_{max})	FWHM	Crystallite size from XRD (nm)	Lattice Parameters		c/a Ratio	Unit cell volume $(Å)^3$
						‘a’ (Å)	‘c’ (Å)		
1	Undoped ZnO	6402	36.291	0.2090	41.70	3.2635	5.2034	1.5944	47.9923
2	0.5% Ag doped ZnO	6456	36.297	0.2065	42.30	3.2813	5.2151	1.5893	48.6364
3	1% Ag doped ZnO	6496	36.321	0.1879	45.63	3.2873	5.2347	1.5924	48.9878
4	2% Ag doped ZnO	6534	36.300	0.1779	47.76	3.2898	5.2415	1.5932	49.1261
5	3% Ag doped ZnO	6567	36.309	0.17778	49.17	3.2915	5.2469	1.5941	49.2276
6	5% Ag doped ZnO	6598	36.315	0.17099	51.12	3.2987	5.2501	1.5916	49.4733

Unit cell volume = a^2 c Sin60°

The measured values of lattice constants for ZnO are a = 3.2635 Å and c = 5.2034 Å, while for Ag-doped ZnO ‘a’ varies from 3.2813 to 3.2987 Å and ‘c’ from 5.2151 to 5.2501 Å as illustrated in Table 1. This increase in lattice parameters is associated with lattice strain caused by difference in ionic radii between zinc and silver ions [32] as described above. However, c/a ratio was found to be nearly constant for all samples. Fig. 3 also depicted shift of (101) peak towards smaller 2θ values when silver was incorporated into interstitial sites and towards larger 2θ values for silver substitution in the ZnO lattice [28].

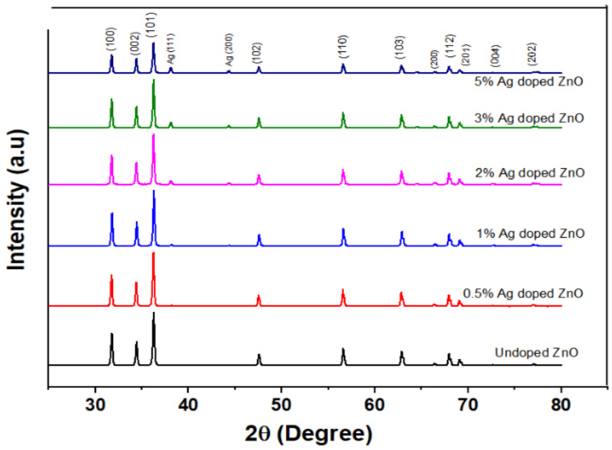

Fig. 2. XRD patterns of ZnO and Ag-ZnO nanoparticles.

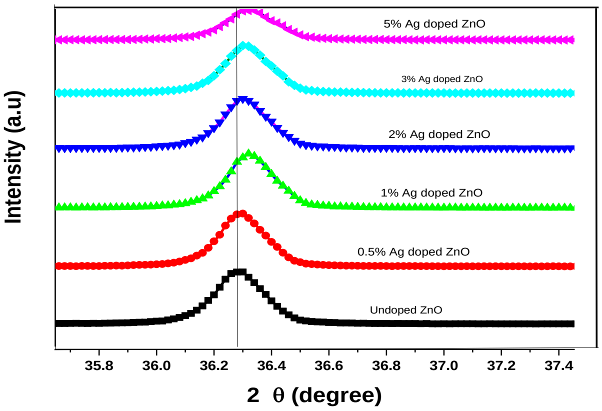

Fig. 3. XRD (101) peak shift in Ag-doped ZnO samples with respect to undoped ZnO.

3.2. Scanning electron microscopy

Fig. 4 demonstrates the surface morphology, size, shape and growth mechanism of ZnO and Ag-ZnO nanoparticles. These SEM images display closely packed nearly spherical and randomly oriented nanoparticles. There appears some enhancement in the porosity and reduction in the density due to liberation of gases which created surface pores and holes [33] as obvious from these images. Undoped ZnO powder consists of nanoparticles with a mean size of about 72 nm. The crystallite/particle size was noted to increase up to ~95 nm for 5%Ag- ZnO nanoparticles. Thus particle size increases as dopant content increases, which is consistent with the XRD results.

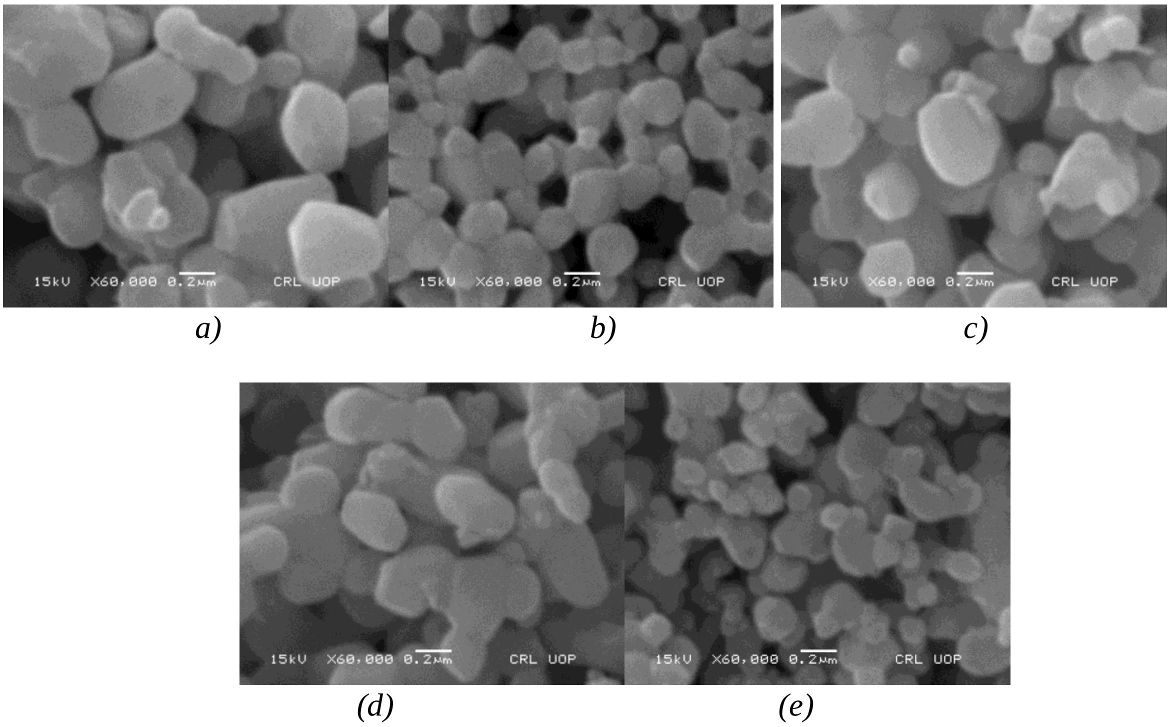

Fig. 4. SEM images for a) pure ZnO, b) 0.05 wt.%, c) 1wt.%, d) 3wt.% and e) 5wt.% Ag-ZnO.

3.3. Optical properties

3.3.1. Diffuse reflectance spectroscopy

To calculate the band gap of ZnO and Ag-ZnO nanoparticles, UV-VIS spectra were investigated in the range of 250-700 nm. It is known that ZnO has a direct band gap, which can be measured from absorbance vs. wavelength (λ) plot (as shown in Fig. 5) using Kubelka-Monk method. The calculated values of band gap energy are tabulated in Table 2, which illustrates that band gap reduces from 3.37 eV to 2.40 eV with rising silver content in the ZnO nanoparticles. Absorbance spectra demonstrates significant shift to larger wavelengths (a red shift) on increasing silver doping due to strong interaction between oxides of Zinc and silver [34]. Such a red shift is expected to occur because of strong interaction between d-electrons of Ag-ions, and s- and p-electrons of the host Zinc oxide [28]. The increment in the particle size and generation of impurity levels with silver concentration as well as enhancement in porosity due to liberation of gases cause enhanced absorbance and result in narrowing the band gap [35, 36]. In addition, as silver is incorporated at the interstitial/substitutional sites in the crystal lattice (as obvious from XRD data), which possibly generates impurity band due to interactions between silver 4d and oxygen 2p orbitals. This might result in pushing Fermi level towards valence band [37]. This decrease in the band gap might also be due to ionic radii difference of Ag and zinc as Ag^+ ions substitutes to Zn^{2+} lattice sites [38].

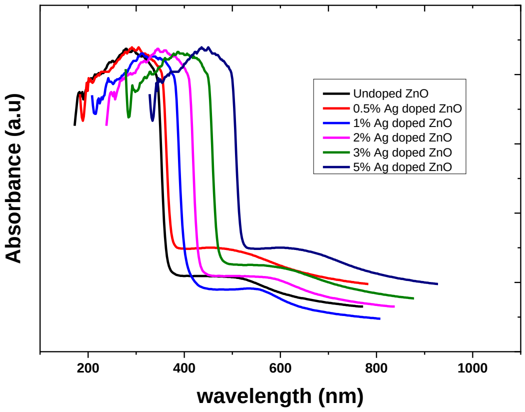

Fig. 5. UV-Visible absorption spectra of undoped and Ag-doped ZnO nanoparticles.

Table 2. Energy band gap Eg of undoped and Ag-doped nanoparticles.

Samples	ZnO	0.05wt% Ag-ZnO	1wt% AgZnO	2wt% Ag- ZnO	3wt% Ag- ZnO	5wt% Ag- ZnO
Energy band gap E= hc/λ=1240/ λ (eV)	3.37	3.29	3.1	2.87	2.62	2.40

3.3.2. Photoluminescence spectra

Photoluminescence spectroscopy is being used for the investigation of chemical composition, structure, impurities and energy transfer. Room temperature PL spectra obtained at excitation wavelength of 325 nm and displayed in Fig. 6 were used to study the influence of silver doping in ZnO nanparticles. Two prominent photoluminescence peaks were observed; one at 390 nm in the UV region due to the recombination rate of electron-hole pairs found in conduction and valence bands, and the other PL peak at 462 nm in the visible region due to intrinsic and extrinsic defects [39]. A decrease in PL intensity was noticed with Ag content. Such a decrease in intensity with silver doping revealed reduction in electron-hole recombination rate due to incorporation of silver at interstitial/substitutional sites, which can generate dual oxygen spaces and produce active surfaces [30]. This result clearly indicates a PL shift to lower photon energy due to a slight shift in wavelength towards higher spectral region. This shows a red shift in UV region, which results in pushing Fermi level towards valence band and narrowing the band gap region [40]. Silver acts as acceptor, which traps the electrons and this leads to reduction in electron-hole recombination rate and hence the PL intensity [41]. Amongst all the samples, 5wt% Ag-ZnO nanoparticles shows the lowest intensity resulting in minimum electron-hole recombination rate due to acceptor role of silver.

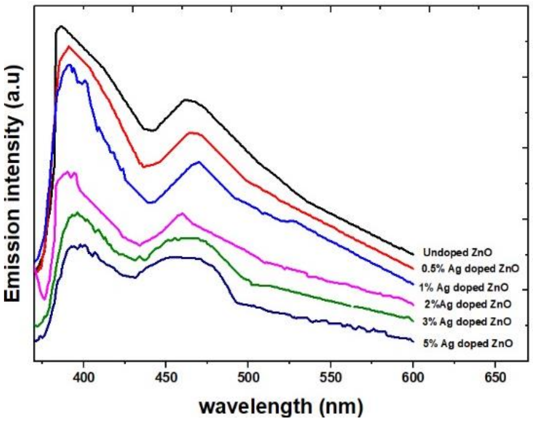

Fig. 6. Room temperature PL emission spectra.

3.4. Dielectric properties

3.4.1. Dielectric constant

Room temperature dielectric properties of ZnO and Ag-ZnO nanoparticles were measured in the frequency range from 20 Hz to 1 MHz using two probe method. The complex dielectric constant, ε^* can be expressed as an entity comprising of real and imaginary parts:

$$\varepsilon^* = \acute{\varepsilon} + j\acute{\acute{\varepsilon}}$$

where $\acute{\varepsilon}$ is its real part of dielectric constant indicating energy stored in the material as a result of polarization and $\acute{\acute{\varepsilon}}$ is the imaginary part of dielectric constant indicating energy loss as heat on the application of an electric field. To find out structural, compositional and intergranular barrier effect, frequency dependent dielectric constant is found by the following relation:

$$\acute{\varepsilon} = \frac{cd}{A\varepsilon_\circ}$$

where "*c*" represents capacitance "*d*" thickness and "*A*" area of the sample, and $\varepsilon_\circ$=8.85 x 10^{-14} F/cm gives permittivity of free space.

Fig. 7 represents log-log plots of real part of dielectric constant $\acute{\varepsilon}$ as a function of frequency f, which indicates decrease in $\acute{\varepsilon}$ with increasing frequency first gradually and then slowly. This decrease in $\acute{\varepsilon}$ might be attributed to the formation of grains which are surrounded by non-conducting grain boundaries. At lower frequencies, high values of $\acute{\varepsilon}$ is expected to be caused by orientation polarization which decreases with the applied frequency [42-43]. Also at low frequencies, charge carriers can easily migrate through the grains, as well as the interface resistance present at the grain boundaries can accumulate itself, which might result in large polarization. The large value of dielectric constant can also be explained on the basis of space charge polarization initiated by inhomogeneities such as porosity, grain structure etc. At higher frequencies, dielectric constant reduces because in this case, charge carriers lag behind the applied ac field and also the polarization reduces [44]. It is also noticed that $\acute{\varepsilon}$ decreases with increasing Ag content in the nanoparticles. This is due to the fact that with rising Ag content in the Ag-doped ZnO system, more and more zinc ions are substituted by silver ions which will reduce the dielectric constant [45].

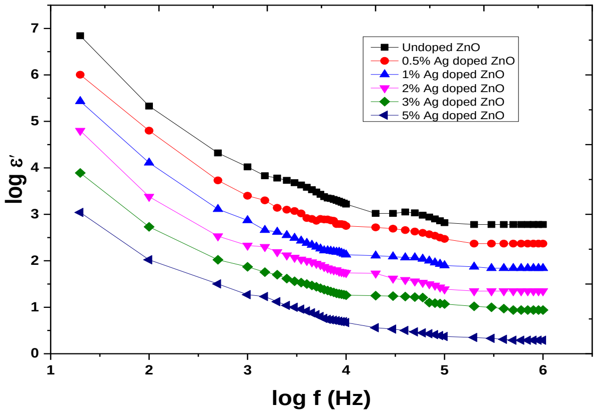

Fig. 7. Dielectric constant of ZnO and Ag-ZnO nanoparticles.

3.4.2. Dielectric loss/ Tangent loss

The dielectric or tangent loss $\acute{\acute{\varepsilon}}$ which describes the loss of energy through heat can be found by

$$\acute{\acute{\varepsilon}} = \acute{\varepsilon} \tan\delta$$

It usually occurs due to the domain wall resonance in a material. It is expected to take place when polarization lags behind applied field due to the presence of impurities and imperfections in a crystal lattice. It is found that porosity has an inverse relation with $\acute{\varepsilon}$ and $\tan\delta$ while density represents a direct relationship [46].

Fig. 8 represents log-log plots of dielectric loss vs. applied ac frequency. These plots appear to be similar to those of dielectric constant (Fig. 7). At lower frequencies, high value of dielectric loss is assumed to be due to orientation of molecules in the direction of applied field by overcoming the internal friction [45]. Also grain boundaries provide resistance due to which some energy is dissipated, which increase the loss. On the other hand, at higher frequencies, the resonance caused by domain walls reduces and more and more molecules become oriented in the direction of an applied field [45] resulting in the reduction of dielectric loss.

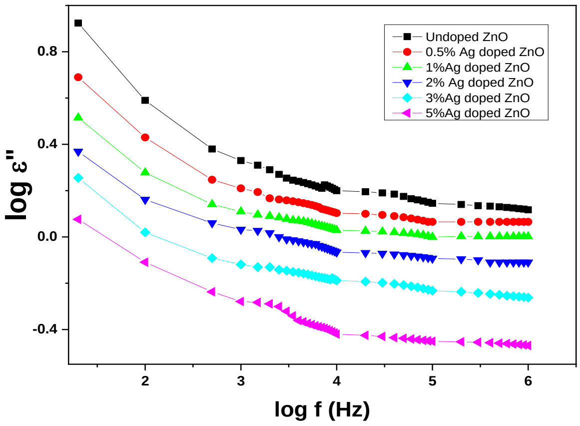

Fig. 8. Dielectric loss in the case of ZnO and Ag-ZnO nanoparticles.

3.4.3. AC conductivity

It is associated with the dielectric constant and the tangent loss through the following relation:

$$\sigma_{ac} = 2\,\pi\,\varepsilon_{\circ}\,\acute{\varepsilon}\,f\,\tan\delta$$

Where ε_o is the permittivity of free space. AC conductivity determined through this relation is plotted as a function of frequency of the applied field as depicted in Fig. 9 for ZnO and Ag-ZnO nanoparticles. It is noted that ac conductivity illustrates a gradual increase with rising frequency. At lower frequencies, because of polarization as well as resistance offered by grain boundaries, conductivity exhibits small magnitudes. But as frequencies rise, there is a decrease in polarization, so conductivity demonstrate an increase in its magnitude. This rise in ac conductivity may also be attributed to the translational hopping process occurring between the localized states as well as due to polaron hopping [45].

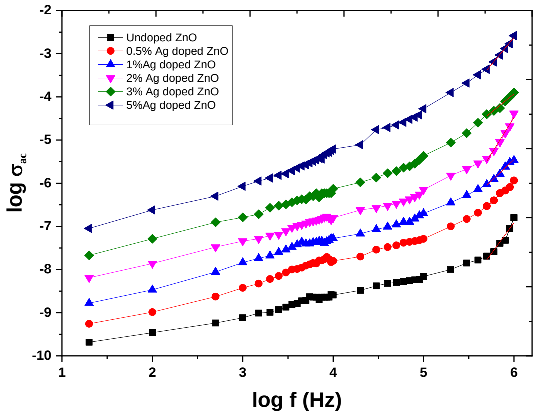

Fig. 9. AC conductivity of ZnO and Ag-ZnO nanoparticles.

3.5. DC electrical conductivity

The DC electrical conductivity of ZnO and Ag-ZnO nanoparticles was measured by two probe method in the temperature range from 27 °C to 125 °C. DC conductivity was determined using the following formula:

$$\sigma \text{ (d.c)} = L / A R$$

where L represents thickness while A area of the sample and R=V/I gives the resistance. Fig. 10 shows Arrhenius plots of Log σ(d.c) vs. 1000/T drawn for undoped and Ag-doped ZnO nanoparticles. These plots illustrate rise in DC conductivity with rising temperature analogous to the temperature dependent behavior of semiconducting materials.

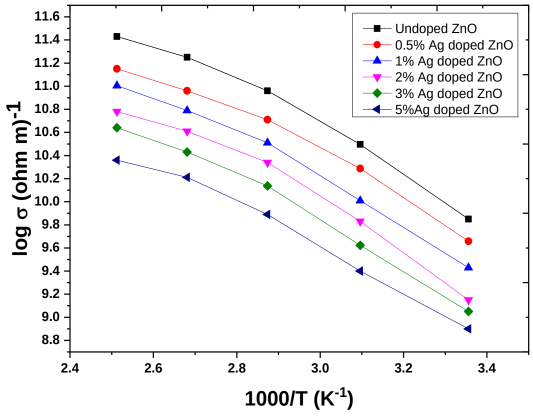

Fig. 10. Changes in DC conductivity versus temperature for ZnO and Ag-ZnO nanoparticles.

This increase in conductivity might be attributed to the presence of defects such as oxygen vacancies and interstitial sites which create impurity bands [47]. In addition, hoping of electrons and holes between adjacent localized states is enhanced with increase in temperature by gaining energy. As soon as an electron is transferred to the adjacent localized site, the neighboring molecules with structural variations respond to this perturbation consequently electron and hole pair is captured momentarily in the potential well resulting in atomic polarization [48]. Electron is expected to stay there until it is thermally excited to the next site. Another possible reason of such hoping phenomenon is that electron or hole is trapped at local defect states, therefore, as temperature increases, more and more electron-hole pairs will be produced by increasing silver content in the ZnO matrix which leads to an increase in conductivity [48].

3.6. Cyclic voltammetry

In order to test the nature of electroactive species inside a semiconducting material, the commonly utilized electroanalytical technique is called cyclic voltammetry. This method can efficiently evaluate the electrode surfaces electrochemically. One of its most common application is the determination of electrochemical characteristics of some electrode material using aqueous solutions of NaOH and/or ferric/ferricyanides [49]. Fig. 11 demonstrates different cyclic voltammograms recorded for both undoped and Ag-doped ZnO nanoparticles inside the 0.1M NaOH at scanning speeds of 5 mV/s, 10 mV/s and 20 mV/s. It can be seen that there exists wider potential windows exhibiting low background currents. These voltammograms demonstrate approximately symmetric peaks which are related with anodic and cathodic behaviors of the nanoparticles based electrode. Such behavior might be associated with the reduction and oxidation occurring at the interface between working electrode and the solution. The cathodic and anodic peaks separation obviously specify the degree of irreversibility in electrochemical reaction occurring at various scan rates. It is noteworthy that this peak separation appears to increase with the rise of Ag content in the ZnO lattice but remains same with rising scan rate.

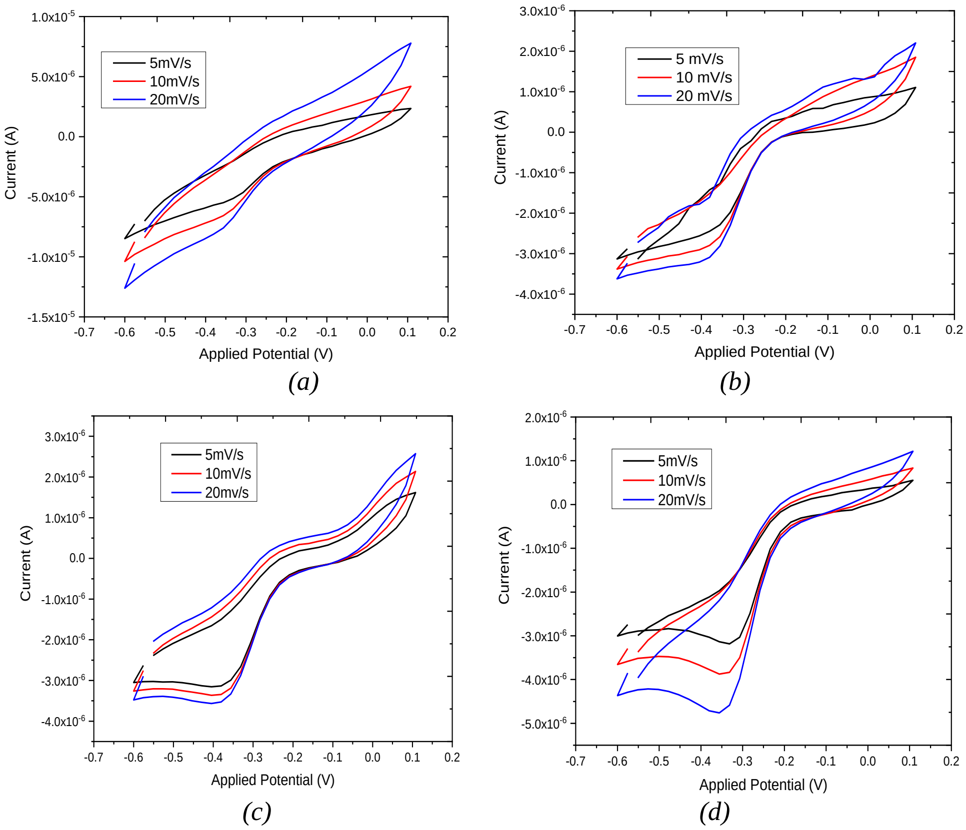

(a) *(b)* *(c)* *(d)*

Fig. 11. Cyclic voltammetry plots for both undoped and Ag-doped ZnO nanoparticles observed at different scan rates as indicated. (a) ZnO, (b) 1 wt.%Ag-ZnO, (c) 3 wt.%Ag-ZnO, (d) 5 wt.%Ag-ZnO.

In pure ZnO nanoparticles, cathodic peaks were observed to appear around -0.29 V while anodic ones around -0.17 V. On the other hand for Ag-doped ZnO samples these peaks were appearing between -0.28 V to -0.25 V and 0.19 V to -0.09 V respectively. This trend leads to a rise in the peak separation, which could be associated with the variations in the transfer of electrons at the interface between working electrode and the solution. Since peak potentials in the case of ZnO and Ag-ZnO are totally different which confirm the incorporation of Ag doping into ZnO nanoparticles [50]. Moreover, there is an increase in the peak height with increasing scan rate, but noticed opposite trend with rising Ag-doping concentration. Such behavior of these voltammograms could be attributed to the oxidation process. The maximum observed value of peak separation is noticed for 3wt.%Ag-ZnO system, which might be caused by high transfer of electrons from Ag to adjacent Zn. Such transfer of electrons represents relatively broader distribution of electrostatic potential which can decrease the potential barrier in the movement of Ag^+ ions improving their migration.

Enhancement in the cathodic peaks with silver doping clarifies that number of electrons incorporated into photocatalysis process enhance with each repeated cycle, confirming an increase in the reaction activity of Ag-ZnO nanoparticles [51]. The electrons and holes produced in the redox reaction move onto photocatalyst surface and generate oxygen species as a result of reaction with adsorbed species. These electrons combine with H^+ to form atomic hydrogen while holes react with water and produce oxygen [52].

4. Conclusions

Auto-combustion technique was employed to synthesize ZnO and Ag-ZnO nanoparticles and the influence of silver doping on the photocatalytic performance for hydrogen production was investigated. The doping of silver into ZnO has significantly influenced the crystallite size, optical properties, photocatalytic performance as well as ac and dc conductivity of ZnO nanoparticles. XRD analysis revealed the invariance of hexagonal wurtzite crystal structure of ZnO upon silver doping with only increase in crystallite size. The DRS demonstrated reduction in band gap energy of ZnO nanoparticles with enhancing silver concentration. The PL studies indicated a red shift in the emission band in Ag-ZnO nanoparticles.

Morphological study by SEM illustrates randomly oriented and closely packed almost spherical nanoparticles of Ag-ZnO. Dielectric measurements for Ag-ZnO revealed opposite variations in dielectric constant and tangent loss with frequency while direct variations for AC conductivity. DC conductivity was enhanced with increase in temperature for silver doped ZnO leading to semiconducting type conduction behavior. The CV study established the fact that redox reaction improved for 5wt.% Ag-ZnO, moreover, anodic and cathodic peaks were observed for all Ag-ZnO systems. The 5 wt% Ag-doped ZnO nanoparticles system elucidates the best photocatalytic behavior for hydrogen production.

Acknowledgement

Authors thank to Dr. Zulfiqar Ahmed shah for technical correction of chemicals names and their formulas.

References

[1] A. Steinfeld, International Journal of Hydrogen Energy **27** (6), 611 (2002).
[2] A. Fujishima, K. Honda, Nature **238** (5358), 37 (1972).
[3] A. Kudo, I. Tsuji, H. Kato, Chemical Communications **17**, 1958 (2002).
[4] D. Zhao, C. F. Yang, Renewable and Sustainable Energy Reviews **54**, 1048 (2016).
[5] X. Hao, Z. Jin, J. Xu, S. Min, G. Lu, Superlattices and Microstructures **94**, 237 (2016).
[6] M. Y. Xie, K. Y. Su, X. Y. Peng, R. J. Wu, M. Chavali, W. C. Chang, Journal of the Taiwan

Institute of Chemical Engineers **70**, 161 (2017).

[7] X. Wang, M. Liu, Z. Zhou, L. Guo, The Journal of Physical Chemistry C **119**(35), 20555 (2015).

[8] R. Chauhan, A. Kumar, R. P. Chaudhary, Archives of Applied Science Research **2**(5), 3782010 (2010).

[9] S. T. Kuo, W. H. Tuan, J. Shieh, S. F. Wang, Journal of the European Ceramic Society **27(**16), 4521 (2007).

[10] B. S. Reddy, S. V. Reddy, N. K. Reddy, Y. P. Reddy, Advanced Materials Letters **5**, 199 (2014).

[11] S. Saravanan, M. Silambarasan, T. Soga, Japanese Journal of Applied Physics **53**(11S), 11RF01 (2014).

[12] R. Mohan, K. Ravichandran, A. Nithya, K. Jothivenkatachalam, C. Ravidhas, B. Sakthivel, Journal of Materials Science: Materials in Electronics **25**(6), 2546 (2014).

[13] C. J. Chang, C. Y. Lin, M. H. Hsu, Journal of the Taiwan Institute of Chemical Engineers **45**(4), 1954 (2014).

[14] C. J. Chang, K. L. Huang, J. K. Chen, K. W. Chu, M. H. Hsu, Journal of the Taiwan Institute of Chemical Engineers **55**, 2 (2015).

[15] C. J. Chang, S. T. Hung, Thin Solid Films **517**(3), 1279 (2008).

[16] Z. M. Shaykhi, A. A. L. Zinatizadeh, Journal of the Taiwan Institute of Chemical Engineers **45(**4), 1717 (2014).

[17] C. J. Chang, E. H. Kuo, Colloids and Surfaces A: Physicochemical and Engineering Aspects **363**(1), 22 (2010).

[18] Y. L. Zhao, H. X. Lu, X. J. Yu, B. B. Fan, D. L. Chen, L. W. Zhang, H. L. Wang, D. Y. Yang, H. L. Xu, R. Zhang, Applied Surface Science **257**(24), 10634 (2011).

[19] G. R. Bamwenda, H. Arakawa, Applied Catalysis A: General **210**(1), 181 (2011).

[20] S. T. Hung, C. J. Chang, M. H. Hsu, Journal of Hazardous Materials **198**, 307 (2011).

[21] M. R. Dhananjeyan, R. Annapoorani, R. Renganathan, Journal of Photochemistry and Photobiology A: Chemistry **109**(2), 147 (1997).

[22] C. Yu, W. Zhou, J. Yu, F. Cao, X. Li, Chinese Journal of Chemistry **30**(3), 721 (2012).

[23] A. S. Weber, A. M. Grady, R. T. Koodali, Catalysis Science & Technology **2**(4), 683 (2012).

[24] S. Peng, R. An, Y. Li, G. Lu, S. Li, International Journal of Hydrogen Energy **37**(2), 1366 (2012).

[25] X. Wang, X. L. Wu, Y. G. Guo, Y. Zhong, X. Cao, Y. Ma, J. Yao, Advanced Functional Materials **20**(10), 1680 (2010).

[26] M. Ahmad, Z. Hong, E. Ahmed, N. R. Khalid, A. Elhissi, W. Ahmad, Ceramics International **39**(3), 3007 (2013).

[27] Joint Committee on Powder Diffraction Standards (JCPDS) File No. 05-0664.

[28] U. P. Gawai, H. A. Khawal, M. R. Bodke, B. N. Dole, In AIP Conference Proceedings **1728**(1), 020607 (2016).

[29] B. D. Cullity, 1979. Elements of X-Ray Diffraction, Addison-Wesley, Boston.

[30] R. S. Zeferino, M. B. Flores, U. Pal, Journal of Applied Physics **109**(1), 014308 (2011).

[31] M. Ahmad, E. Ahmed, Y. Zhang, N. R. Khalid, J. Xu, M. Ullah, Z. Hong, Current Applied Physics **13**(4), 697 (2013).

[32] C. Karunakaran, V. Rajeswari, P. Gomathisankar, Journal of Alloys and Compounds **508**(2), 587 (2010).

[33] S. Suwanboon, Science Asia **34**(1), 31 (2008).

[34] S. Singh, M. Arora, Proceedings of the Workshop on Architectural and System Support for Improving Software Dependability, New Delhi, India (2006) 501-504).

[35] O. J. Perales-Perez, M. S. Tomar, S. P. Singh, A. Watanabe, T. Arai, A. Kasuya, K. Tohji, Physica Status Solidi (c) **1**(4), 803 (2004).

[36] C. S. Lin, C. C. Hwang, W. H. Lee, W. Y. Tong, Materials Science and Engineering: B, **140**(1), 31 (2007).

[37] T. Pauporté, O. Lupan, J. Zhang, T. Tugsuz, I. Ciofini, F. Labat, B. Viana, ACS Applied Materials & Interfaces **7**(22), 11871 (2015).

[38] S. H. Jeong, B. N. Park, S. B. Lee, J. H. Boo, Surface and Coatings Technology **193**(1), 340

(2005).
[39] F. Xu, Y. Yuan, D. Wu, M. Zhao, Z. Gao, K. Jiang, Materials Research Bulletin, **48**(6), 2066 (2013).
[40] A. S. Menon, N. Kalarikkal, S. Thomas, Indian Journal of NanoScience **1**(1), 16 (2013).
[41] N. R. Khalid, Z. L. Hong, E. Ahmed, Y. W. Zhang, H. Chan, M. Ahmad, Applied Surface Science **258,** 5827 (2012).
[42] M. Levin, M. Miller, Uspekhi Fizicheskikh Nauk **135**(3), 425 (1981).
[43] K. W. Wagner, Annalen der Physik **345**(5), 817 (1913).
[44] S. A. Ansari, A. Nisar, B. Fatma, W. Khan, A. H. Naqvi, Materials Science and Engineering: B **177**(5), 428 (2012).
[45] S. Sagadevan, K. Pal Z. Z. Chowdhury, M. E. Hoque, Journal of Sol-Gel Science and Technology 1 (2017).
[46] A. K. Roy, A. Singh, K. Kumari, K. Amar Nath, A. Prasad, K. Prasad, ISRN Ceramics, (2012).
[47] A. Sawalha, M. Abu-Abdeen, A. Sedky, Physica B: Condensed Matter **404**(8), 1316 (2009).
[48] M. S. Hossain, R. Islama, K. A. Khan, Chalcogenide Letters **5**(1), 1 (2008).
[49] R. Torz-Piotrowska, A. Wrzyszczyñski, K. Paprocki, M. Szreiber, C. Uniszkiewicz, E. Staryga, Journal of Achievements in Materials and Manufacturing **37,** 486 (2009).
[50] M. Maruthupandy, M. Anand, G. Maduraiveeran, S. Suresh, A. S. H. Beevi, R. J. Priya, Advances in Natural Sciences: Nanoscience and Nanotechnology **7**(4), 045011 (2016).
[51] X. Xia, J. Tu, Y. Zhang, X. Wang, C. Gu, X. B. Zhao, H. J. Fan, ACS Nano **6**(6), 5531 (2012).
[52] K. S. Kumara, H. P. Nagaswarupa, K. V. Mahesh, S. C. Prashantha, M. Mylarappa, D. M. K. Siddeshwara, Nanosystems: Physics, Chemistry, Mathematics **7**(4), 662 (2016).